Journal of Molecular Modeling (2024) 30:191
https://doi.org/10.1007/s00894-024-05994-1

ORIGINAL PAPER

Unveiling the potential of graphene and S-doped graphene nanostructures for toxic gas sensing and solar sensitizer cell devices: insights from DFT calculations

S.A.A. Alsaati[1] · Rabab Saadoon Abdoon[2] · Eman Hamid Hussein[3] · Hayder M. Abduljalil[2] · Rajaa K. Mohammad[4] · Mohammed A. Al-Seady[5,6] · Ansaf N. Jasim[6] · Noor Al-Huda Saleh[2] · Lynet Allan[7]

Received: 21 April 2024 / Accepted: 24 May 2024 / Published online: 29 May 2024

Abstract

Context In this work, we explore the potential of 2D materials, particularly graphene and its derivatives, for eco-friendly electricity generation and air pollution reduction. Leveraging the significant surface area of graphene nanomaterials, the susceptibility of these graphene-based nanostructures to hazardous substances and their applicability in clean solar cell (SSC) devices were systematically investigated using density functional theory (DFT), as implemented within Gaussian 5.0 code. Time-dependent DFT (TD-DFT) was employed to characterize the UV-visible spectrum of unstrained nanostructures. Herein, we considered three potentially harmful gases—CO, NH3, and Br2. Adsorption calculations revealed a notable interaction between the pure graphene nanostructure and Br2 gas, while the S-doped counterpart exhibited reduced interaction. Saturated S-doped nanostructures demonstrated an enhanced affinity for NH3 and CO gases compared to their pure S-doped counterparts, attributed to the sulfur (S) atom facilitating gas molecule binding to the nanostructure's surface. Furthermore, simulations of the SSC device architecture indicated the superior performance of the pure graphene nanostructure in terms of light-harvesting efficiency, injection energy, and electron injection into the lower conduction band of CBM titanium dioxide (TiO_2). These findings suggest a potential avenue for developing nanostructures tailored for SSC devices and gas sensors, offering a dual solution to address air pollution concerns.

Methods Density function theory was used to compute the ground and excited state properties for pure and sulfur-doped graphene nanostructures. The hybrid function B3LYP with a 6–31G* basis set was utilized to describe the exchange correlation. Gauss Sum 2.2 software is used to estimate the density of state (DOS) for all structures under investigation.

Keywords Density function theory (DFT) · Solar sanitizer cell (SSC) · Graphene · Graphene-sulfide · Nanostructures

Introduction

In recent decades, environmental pollution has been considered one of the most dangerous issues worldwide. As a result, researchers have been striving to find many solutions to this problem [1, 2]. Pollution has many sources, such as gas emissions from cars, factories, and solid waste. Because air pollution is harmful to human health and the environment, researchers have developed many effective methods to remove or decrease it [3]. They have developed devices

✉ Mohammed A. Al-Seady
Al-Saadi.Mohammed.Ayad.Mejbel@stud.u-szeged.hu; wellmsc@gmail.com

1 College of Basic Education, University of Babylon, Babylon City 51002, Iraq

2 Physics Department, College of Science, University of Babylon, Babylon City 51002, Iraq

3 Physics Department, College of Education for Pure Science, University of Babylon, Babylon City 51002, Iraq

4 Department of Physics, College of Science, University of Kerbala, Kerbala City 56001, Iraq

5 Department of Theoretical Physics, University of Szeged, Tisza Lajos krt. 84-86, Szeged City 6720, Hungary

6 Environmental Centre and Research Studies, University of Babylon, Babylon City 51002, Iraq

7 Department of Physics, Faculty of Science and Technology, University of Nairobi, P.O.Box 30197-00100, Nairobi, Kenya

with high selectivity for gas molecules in the environment, as well as high response times and recovery rates. Over the past two decades, low-dimensional materials have gained significant interest for applications like effective gas sensor devices due to their higher surface area [4]. Graphene is considered one of the most well-known two-dimensional materials, discovered by Geim and Novoselov at the Manchester Laboratory of Nanotechnology [5]. Following the discovery of graphene, new types of materials have been derived, such as germanene, silicene, zinc oxide, boron nitride, transition metal dichalcogenides, and aluminum nitride [5–9]. The honeycomb lattice of two-dimensional materials endows them with remarkable electronic, optical, magnetic, and geometrical properties, primarily due to quantum size effects [10, 11]. These materials have many applications, including photocatalysis, energy conversion, and the fabrication of nanoelectronic devices, attributed to the planar surface properties of two-dimensional materials [12–14]. However, graphene has several disadvantages, such as high toxicity and an incomplete band gap energy. Due to these issues, researchers have considered other types of materials, such as graphene structures fabricated from group 4 atoms of the periodic table, especially tin (Sn) atoms [15, 16]. Despite the many advantages of graphene, the physical adsorption of gas molecules on its surface reduces its importance for application in gas sensor nano-devices [17, 18]. Various strategies have been proposed to improve the sensing properties of graphene-based gas sensors, either by doping graphene with metal atoms or by creating defects in the graphene lattice by removing some atoms from specific positions [17, 19–21].

A monolayer of graphene consists of a single layer of carbon atoms arranged in a 2D honeycomb lattice structure [22–24]. The carbon atoms in monolayer graphene form a 2D plane by bonding with three neighboring atoms [25]. The edges of monolayer graphene can exhibit either an armchair or zigzag configuration [26]. The in-plane carbon-carbon bonds in graphene are explained by sp^2 hybridization [27]. The fourth electron of each carbon atom forms a π-bond, enabling the exchange of electrons over the surface of the material [28]. This is because the carbon atom's valence shell has four electrons but is only bonded to three surrounding carbon atoms.

The bonding of these electrons creates a unique valence and conduction band structure, which is distinctive to graphene. Interestingly, the valence and conduction bands of graphene intersect at the Fermi level, thereby creating Dirac points [29, 30]. Consequently, a pure monolayer of graphene has a zero band gap between its energy levels. This unique nature of graphene's electronic bands makes it useful for multiple applications [31, 32]. However, it is possible to alter the electronic structure and induce band gaps in graphene through various techniques such as stacking multiple layers, applying strain, or introducing limited graphene layers [33] or defects [34, 35].

Graphene has been extensively studied in both scientific and industrial research as an effective sensing material for a wide variety of molecules, ranging from gases to minuscule bioactive substances [36]. Even basic graphene-based sensors can detect changes in conductivity caused by the adsorption of analyte molecules [37]. The adsorbed gas molecules can alter the concentration of charge carriers in graphene, thereby affecting its conductivity. There is a hypothesis that such devices may have the capability to detect single molecules [38]. To fully harness the potential of graphene sensors, it is crucial to understand the dynamics between the graphene surface and the adsorbed molecules [39]. The adsorption of small molecules on graphene has been the focus of theoretical research [40].

Previous studies mainly investigated pristine graphene and estimated relatively low adsorption energies, which were insufficient for gas-sensing applications[41]. With the depletion of fossil fuels and increasing environmental concerns, there has been a growing interest in exploring renewable and environmentally friendly energy sources [42]. Dye-sensitized solar cells (DSSCs) have emerged as a promising clean and renewable energy solution due to their high photoelectronic absorption efficiencies and cost-effective manufacturing methods [43]. DSSCs have been considered a viable alternative to conventional silicon-based solar cells, thanks to their ease of fabrication and potential for large-scale production [44]. However, to effectively harness solar energy and transport electrons in DSSCs, highly efficient sensitizers are required [45].

Tools and methods

The structure, electrical properties, and optical features of pure graphene and sulfur-doped nanomaterials is investigated using density functional theory (DFT) calculations. Ground state computations were utilized to determine the relative orientation of gas molecules on the surfaces of the nanomaterials. The ground state calculations involved energy gap, molecular orbital energy, and adsorption energy. A density functional theory program was employed to estimate all the relevant ground state properties. Additionally, time-dependent density functional theory (TD-DFT) is used to determine the UV-visible spectrum, which aided in identifying the maximum absorption wavelength. B3LYP hybrid function is used to describe the exchange-correlation at the level of theory 6-31G*. Gaussian version 09 simulation software was utilized for the implementation of all relevant properties. The spin was treated by the closed shell method and the systems were described by a single spin state. Nanotube modular software is used to generate the graphene nanostructures, the input parameters of the graphene nanostructure (*n*, *m*, and *L*) are (5, 5, 16), *n*, *m*, and *L* refer to the charity and length of graphene nanostructure, respectively. Gaussian View (5.0) is utilized to visualize the nanostructures and generate the input files.

Theoretical concepts

The quality of a clean solar cell (SSC) device is often assessed by its conversion efficiency of incident light, known as the incident photon-to-current conversion efficiency (IPCE). IPCE is influenced by several factors, including the efficiency of charge collection (η_e), the efficiency of electron injection (γ_inj), and the light harvesting efficiency (LHE). The equations for IPCE and LHE are as follows [46]:

$$\text{IPCE} = \text{LHE} * \Phi_{inje} * \eta_c \tag{1}$$

$$\text{LHE} = 1 - 10^{-f} \tag{2}$$

Where f is the oscillation strength corresponding to the maximum wavelength of absorption, Φ_{inje} is related to the free energy of electron injection [47].

$$\Phi_{\text{injection}} \propto f\left(-\Delta G_{(\text{Injection})}\right) \tag{3}$$

From Eq. 3 indicated that the more negative energy of $\Delta G_{(\text{Injection})}$, the greater the electron injection.

$\Delta G_{(\text{Injection})}$ is the difference between the oxidation potential of the excited state ($E_{OX}^{SSC^*}$) and the reduction potential of TiO_2 conduction band (CBM), which can explain as [48]:

$$\Delta G_{(\text{Injection})} = E_{OX}^{SSC^*} - \text{ECBM}_{(TiO_2)} \tag{4}$$

CBM is minimum conduction band of TiO_2, and it is equal − 4.00 or − 4.30 eV, in the same method $E_{OX}^{SSC^*}$ can be estimated by the following formula:

$$E_{\text{OX}}^{\text{SSC}^*} = E_{\text{OX}}^{\text{SSC}} - \Delta E \tag{5}$$

Where $E_{\text{OX}}^{\text{SSC}}$ (-E_{HOMO}) is the ground state oxidation potential of the SSC device, ΔE is the lowest absorption energy corresponding to the maximum wavelength of absorption [49].

The free energy of electron regeneration ($\Delta G_{(\text{Regenaeration})}$) can be computed by the following formula [50]:

$$\Delta G_{(\text{Regeneration})} = E_{\text{ox}}^{\text{SSC}} - E_{\text{redox}}^{\text{electrolyte}} \tag{6}$$

Where the term $E_{\text{redox}}^{\text{electrolyte}}$ represent the redox potential of iodine/tri-iodine (I/I_3) electrolyte is equal (− 4.85 eV) [51].

According to relation between the open-voltaic circuit and the SSC (E_{LUMO}) based on injected electron from the HOMO level to $\text{CBM}_{(\text{TiO2})}$ given by the following relation [52]:

$$V_{\text{OC}} = E_{\text{LUMO}} - \text{ECBM}_{(TiO_2)} \tag{7}$$

The adsorption energy can be calculated from the following equation[53]:

$$E_{\text{Ads}} = E_{\text{Complex}} - \left(E_{\text{Gas}} + E_{\text{Rib}}\right) \tag{8}$$

Where E_{Complex} E_{Gas}, and E_{Rib} are the total energy of the interacted system, gas molecule and isolated ribbon respectively [54].

The sensitivity (S) of graphene and S-doped nanostructures can be evaluated by the following relation [35]:

$$S = \frac{E_0}{\left(E_{1\_}E_0\right)}\% \tag{9}$$

Where (E_0) and (E_1) represent the energy gap of the graphene and S-doped nanostructure in the absence and present gas molecular, respectively.

The thermodynamic formation energy can be computed by the following relation [55]:

$$E_f = \left[E_{GS} - E_G\right] - n\left[E_C - E_H\right] - mE_S \tag{10}$$

Where E_{GS}, E_G are refer to total energy for GS and G nanostructures, $E_C - E_H$, E_S, are represent the total energy for C, H and S atoms, and n and m refer to the number of C, H, and S atoms respectively.

Relaxation structure for pure and S-doped graphene nanostructures

The geometry relaxation of graphene (G) and S-doped graphene (GS) nanostructures in an isolated phase was computed using the B3LYP functional at the 6–311G level. Figure 1 illustrates the geometrical structure for both the isolated and interaction phases of the pure and S-doped graphene nanostructures. Table 1 lists the bond lengths and bond angles of the (G) and (GS) nanostructures, respectively. The results of the relaxation calculations showed that the G nanostructure has four bond types: C–C, C=C, C≡C, and C–H [56]. Additionally, after replacing four carbon atoms with four sulfur (S) atoms, a new bond appeared the C–S bond, which was bonded with three neighboring carbon atoms [57].

After the interaction between gas molecules and the surface of G and GS nanostructures, the results showed that some types of curvature appeared, especially when Br_2, CO, and NH_3 were adsorbed on the surface of the GS nanostructure. The curvature appears due to the high interaction between the gas molecules and the surface of the GS

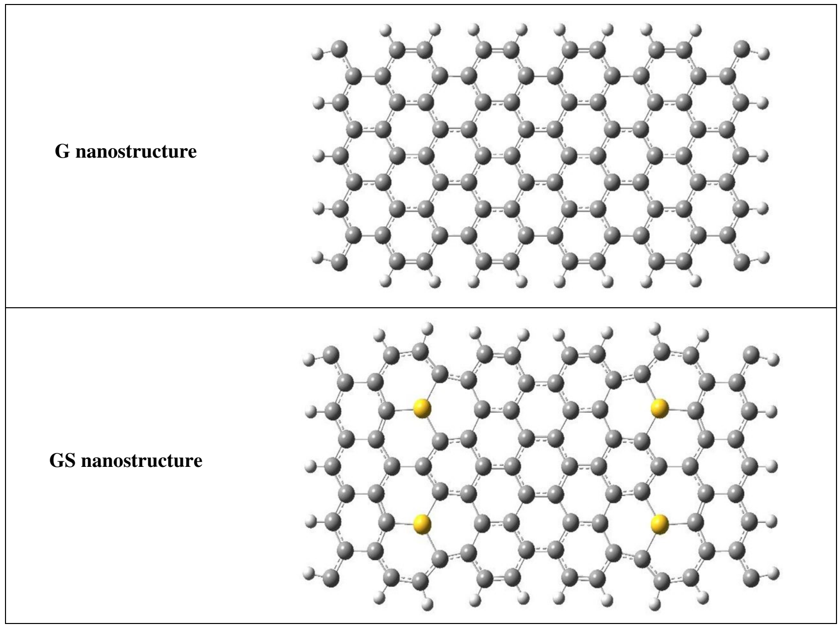

Fig. 1 The geometrical structures for G and GS nanostructures, the white, gray, and yellow balls represented hydrogen, carbon, and sulfur atoms, respectively

Table 1 The geometrical parameters for G and GS nanostructures measured via the DFT method

Nanostructures	Bond types	Bond length (Å)	Angle types	Angle length (Deg.)
G	$C-C$	1.4511–1.4651	$C-C\cdots C$	119.2975–122.2845
	$C=C$	1.3765–1.3814	$C\cdots C\cdots C$	119.8576–123.0464
	$C\cdots C$	1.4207–1.4335	$C\cdots C-H$	107.4517–119.9180
	$C-H$	1.0835–1.1175	$C=C\cdots H$	117.9782–121.9335
			$C=C\cdots C$	120.7507–121.5643
GS	$C-S$	1.7223–1.7743	$C-S-C$	117.7060–122.3631
	$C-C$	1.4649–1.7827	$S-C\cdots C$	108.5255–116.0649
	$C=C$	1.3633–1.3835	$S-C=C$	114.8007
	$C\cdots C$	1.3943–1.4371	$C-C\cdots C$	117.6497–127.6279
	$C-H$	1.0864–1.1168	$C\cdots C\cdots C$	122.8359–144.6686
			$C\cdots C-H$	108.3997–120.9002
			$C-C-C$	126.2033
			$C=C\cdots C$	121.9172–134.7997

nanostructure, in addition to the high reactivity of the S atom. The computed results of geometrical relaxation indicated that the bond angles changed during the adsorption of gas molecules on the surface of the nanostructure, which was clearly observed in the Br_2/GS interaction. The interaction of gas molecules with the surface of the G nanostructure did not affect the nature of the surface, and it remained planar. The geometrical calculations showed that the angle between the three neighboring carbon atoms and the sulfur atom reduced to 100.44°–102.30° compared with the isolated state. The relaxation calculations showed that all computed bond lengths and bond angles were in agreement with previous studies[53, 58, 59].

The thermodynamic formation energy (E_f) is considered one of the important properties to evaluate the chemical stability of the nanostructures, (E_f) is computed based on Eq. (10). The calculation showed that, the formation energies for the graphene and S-doped nanostructures are −29.1954 and −41.8425 eV/atom, respectively. As an evaluated result, both systems have high chemical stability especially the S-doped graphene nanostructure (GS). In addition, doped graphene by four sulfur (S) atoms enhance it thermodynamics stability, so that their potential ability for synthetic purposes [55].

Pollution reduction

In this section, we will investigate the interaction between toxic gas molecules and the surfaces of G and GS nanostructures.

Adsorption energy

The adsorption energy calculation for adsorbed gas molecules on the surfaces of G and GS nanostructures is discussed in this section. A DFT tool was utilized to compute the interaction energy between adsorbed gas molecules and the surfaces of G and GS nanostructures at the 6–31G level with the B3LYP hybrid functional. Figure 2 demonstrates the fully optimized structure for the interaction between gas molecules and the surfaces of G and GS nanostructures. Furthermore, the adsorption energy and molecular distance are listed in Table 2. For the G nanostructure, the maximum adsorption energy observed when Br_2 adsorbed on the surface was around − 185.796 eV, with a molecular distance of 3.21 Å. Additionally, the adsorption energy of the CO gas molecule was observed around − 3.8721 eV. It was also noted that a double bond appeared between the carbon atom of the G nanostructure and the CO gas molecule [60]. The results deduced that the chemical adsorption between CO and the G nanostructure occurred due to the formation of a chemical bond between them. Conversely, weak physisorption was observed when the NH_3 gas molecule adsorbed on the surface of the G nanostructure, with an adsorption energy of around − 0.099 eV and a molecular distance of approximately 3.84 Å. Moreover, the most suitable

Table 2 The adsorption energy and molecular distance for the adsorption process between the surface of G nanostructure and gas molecule measured by the DFT method

Nanostructures	Adsorption energy (eV)	Molecular distance (Å)
G/CO	− 3.872	1.35
G/NH_3	− 0.099	3.84
G/Br_2	− 185.796	3.21

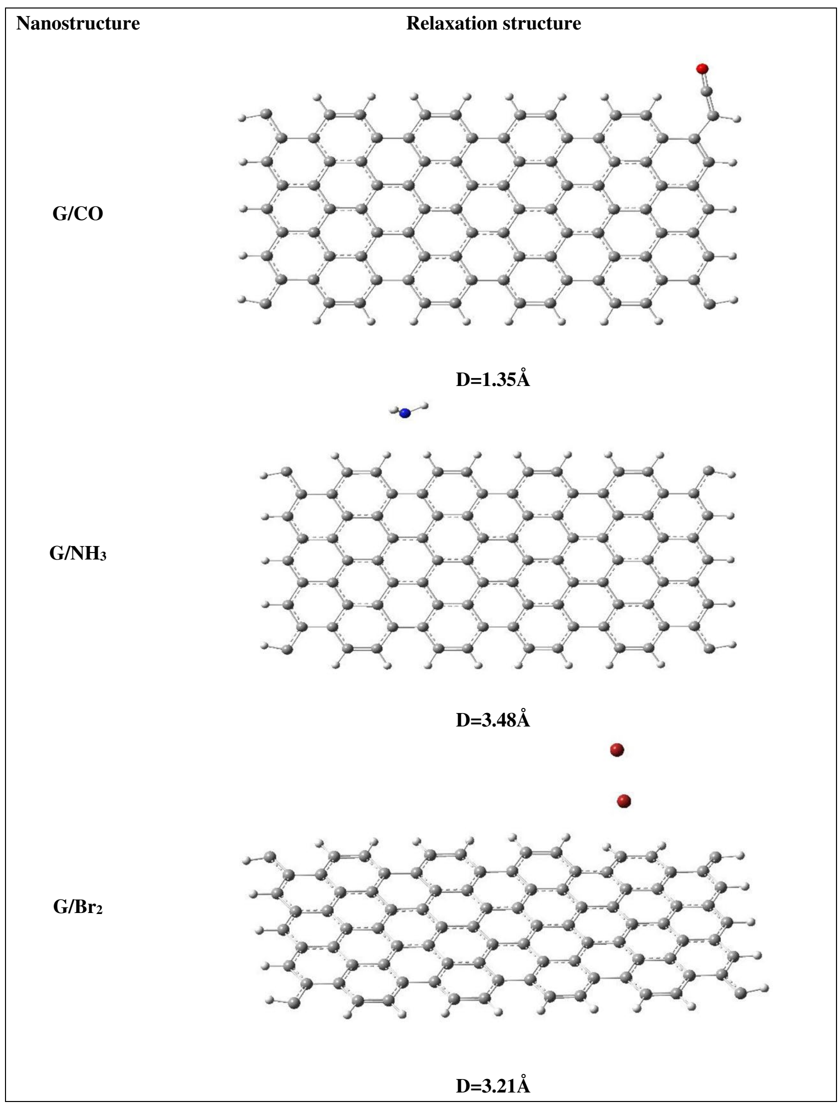

Fig. 2 The figure illustrates the most suitable configuration between the surface of G nanostructure and interacted gas molecules. D represents the distance between the gas molecule and the surface of G nanostructure. Green, red, and dark red balls represent nitrogen, oxygen, and bromine atoms respectively

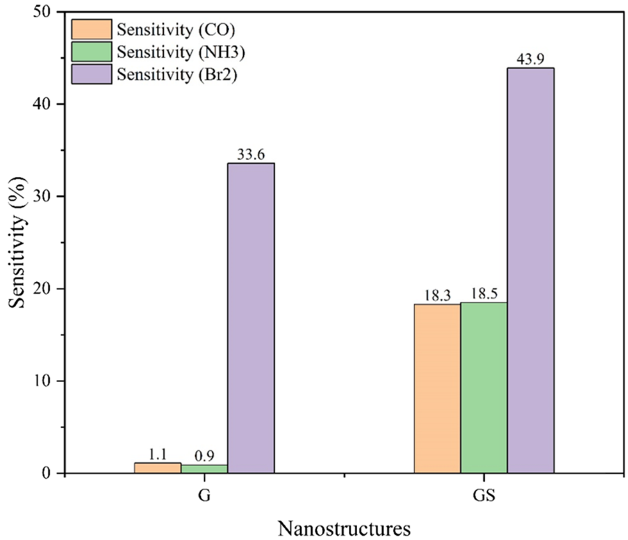

Fig. 3 The bar chart of the sensitivity property for the graphene (G) and S-doped (SG) nanostructures

Table 3 The table indexed the adsorption energy and molecular distance for the adsorption process between the GS nanostructure and gases molecule computed vis DFT tool

Nanostructures	Adsorption energy (eV)	Molecular distance (Å)
GS/CO	− 9.306	2.65
GS/NH_3	− 9.377	2.29
GS/Br_2	− 40.274	2.95

configuration showed that NH_3 and Br_2 were located above the site of the carbon ring, whereas CO was observed at the edge of the G nanostructure.

Besides the adsorption energy calculations, the sensitivity property is another essential parameter for explaining the ability of graphene nanostructures to sense gas molecules. Figure 3 shows the bar chart of the sensitivity property of the graphene and S-doped nanostructures, computed based on Eq. (9). From the figure, graphene has a high sensitivity to the Br_2 gas molecule, around 33%. This result agrees with the adsorption calculations. Additionally, the evaluated outcome indicated that graphene nanostructures had lower sensitivity toward CO and NH_3 gas molecules.

The corresponding adsorption energy results for the SG nanostructure are listed in Table 3. The results show that the adsorption energy of CO and NH_3 improved. For example, the adsorption energy of CO enhanced from − 3.872 eV to − 9.306 eV. However, the interaction energy of Br_2 reduced when it was adsorbed on the surface of the SG compared to its adsorption on the G nanostructure. Moreover, the curvature in the SG nanostructure plays an essential role in improving the interaction energy between gas molecules and the surface. The molecular distance between gas molecules and the surface of the SG nanostructure was closer compared to the G nanostructure, except for the adsorption of CO on the surface of the SG nanostructure. Finally, doping the graphene nanostructure with sulfur atoms improves the interaction energy and induces some types of curvature. These curvatures are essential mechanisms for enhancing the electronic and optical properties of the graphene nanostructure, which will be investigated in the next sections. Figure 4 illustrates the most suitable configuration between the surface of the GS nanostructure and gas molecules. As shown in Fig. 4, the sensitivity of the graphene nanostructure toward CO and NH_3 gas molecules is modified due to the effect of S atoms. Furthermore, due to the high adsorption energy between gas molecules and the surface of the sulfur-doped graphene nanostructure, the energy gap becomes open. In addition, the results showed that the sulfur-doped graphene nanostructure had a high ability to detect the Br_2 gas molecule. As shown in the figure, the sensitivity to Br_2 was modified to about 43%.

Frontier orbital and energy gap

Frontier orbitals provide detailed information about the interaction between the highest occupied molecular orbitals (HOMO) and lowest unoccupied molecular orbitals (LUMO) [61, 62]. The main aim of studying the Frontier Molecular Orbitals (FMOs) is to understand chemical interactions and to develop new semiconductor materials [1, 63]. According to the molecular orbitals hypothesis, the HOMOs act as electron donors, while the LUMOs act as electron acceptors. The difference between HOMO-LUMO defines an energy gap (Eg) property[12]. The energy gap property is an important parameter to understand the conductivity, stability, and reactivity of semiconductor materials. Moreover, the energy gap is used to assess the selectivity, sensitivity, and reactivity, as well as many other essential properties of adsorbed materials [64]. A higher energy gap value describes semiconductor stability, while a lower energy gap value indicates higher reactivity. Tables 4 and 5 list the computed values of the FMOs and Eg for G and GS nanostructures adsorbed with gas molecules, respectively, achieved utilizing the 6–31G basis set at the B3LYP functional level. For the G nanostructure adsorbed with gas molecules, it was observed that the surface had a high energy gap when CO and NH_3 were adsorbed, while no changes in the energy gap of the G nanostructure were observed when gas molecules were adsorbed. Conversely, when Br_2 was adsorbed on the surface of the G nanostructure, the energy gap shrunk from 1.992 eV to 1.321 eV, indicating that the surface had higher reactivity with Br_2 compared to CO and NH_3. Finally, the

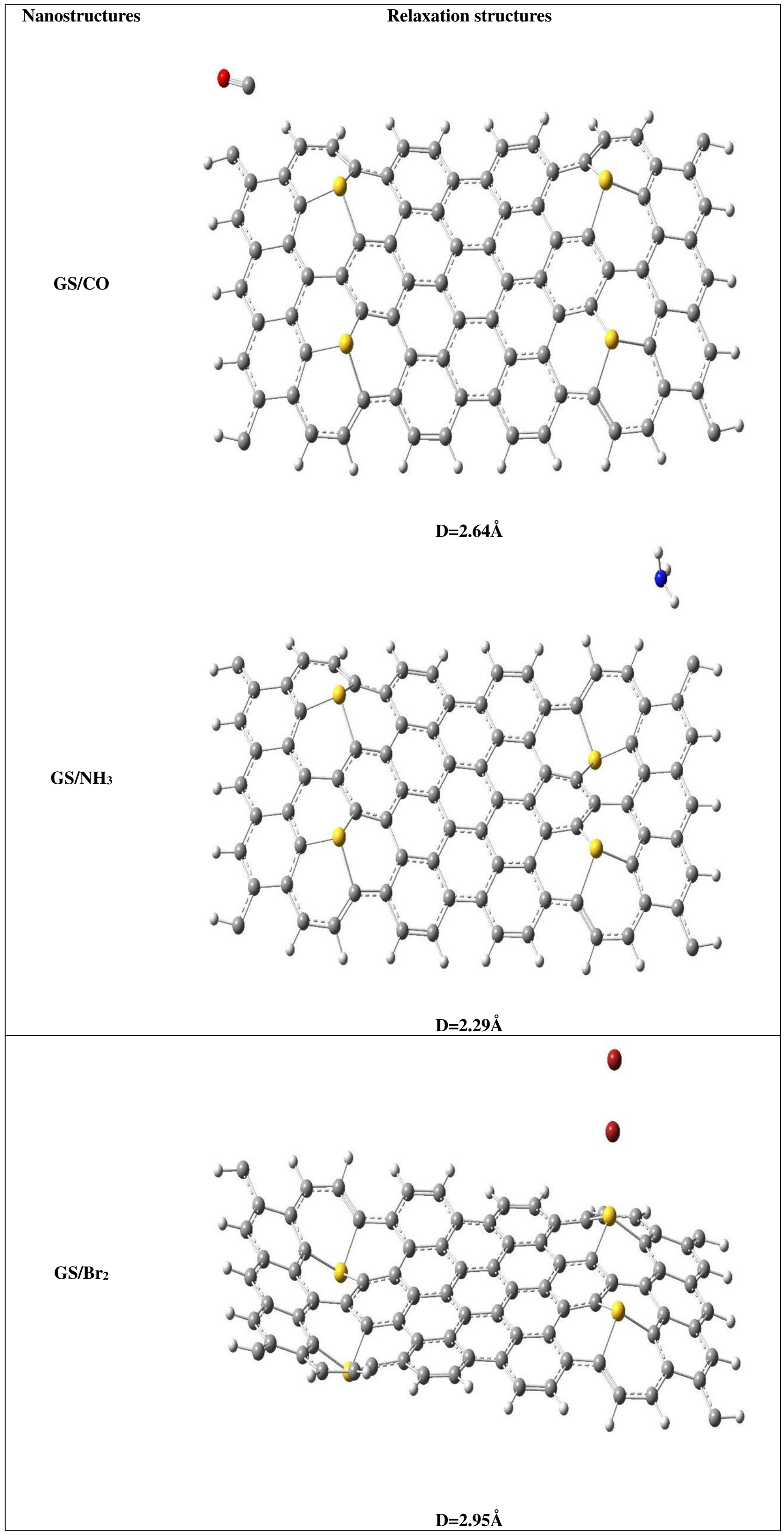

Fig. 4 The most relaxation structure for the adsorption process between the surface of GS nanostructure and gas molecules

Table 4 The table indexed the frontier molecular orbitals (FMOs) and energy gap (E_g) for adsorbed CO, NH_3, and Br_2 on the surface of G nanostructure measured in the electron volt unit (eV)

Nanostructure	HOMO	LUMO	E_g
G	− 5.202	− 3.210	1.992
G/CO	− 5.129	− 3.156	1.972
G/NH_3	− 5.129	− 3.118	1.973
G/Br_2	− 5.326	− 4.005	1.321

Table 5 The frontiers orbitals (FMOs) and energy gap (E_g) results of the graphene-S-doped (GS) nanostructure adsorbed with gas molecules measured in eV unit

Nanostructures	HOMO	LUMO	E_g
GS	− 5.099	− 3.367	1.732
GS/CO	− 5.017	− 3.603	1.414
GS/NH_3	− 4.971	− 3.560	1.411
GS/Br_2	− 4.841	− 3.865	0.976

high chemical interaction between the surface of the G nanostructure and Br_2 gas molecule caused the shrinkage in the energy gap value.

Figure 5 illustrates the density of states (DOS) spectrum for the adsorption process between the G nanostructure and gas molecules, computed by GaussSum 2.2 software. The main idea of the DOS spectrum is to indicate the shift in the Frontier Molecular Orbitals (FMOs). The DOS spectrum is plotted in the range of − 10 to 4 eV. From the figure, it is observed that the HOMO level has a slight shift to higher energy when CO and NH_3 are adsorbed, whereas the HOMO level shifts to lower energy when Br_2 is adsorbed on the surface of the G nanostructure. Moreover, the LUMO level exhibits the same behavior when gas molecules are adsorbed on the surface of the G nanostructure, for example, it has a slight shift to higher energy when CO and NH_3 are adsorbed.

For the adsorption of gas molecules on the SG nanostructure, the DFT calculations showed that the energy gap of GS was reduced. Lower energy gap values were observed when the Br_2 gas molecule adsorbed on the surface of GS.

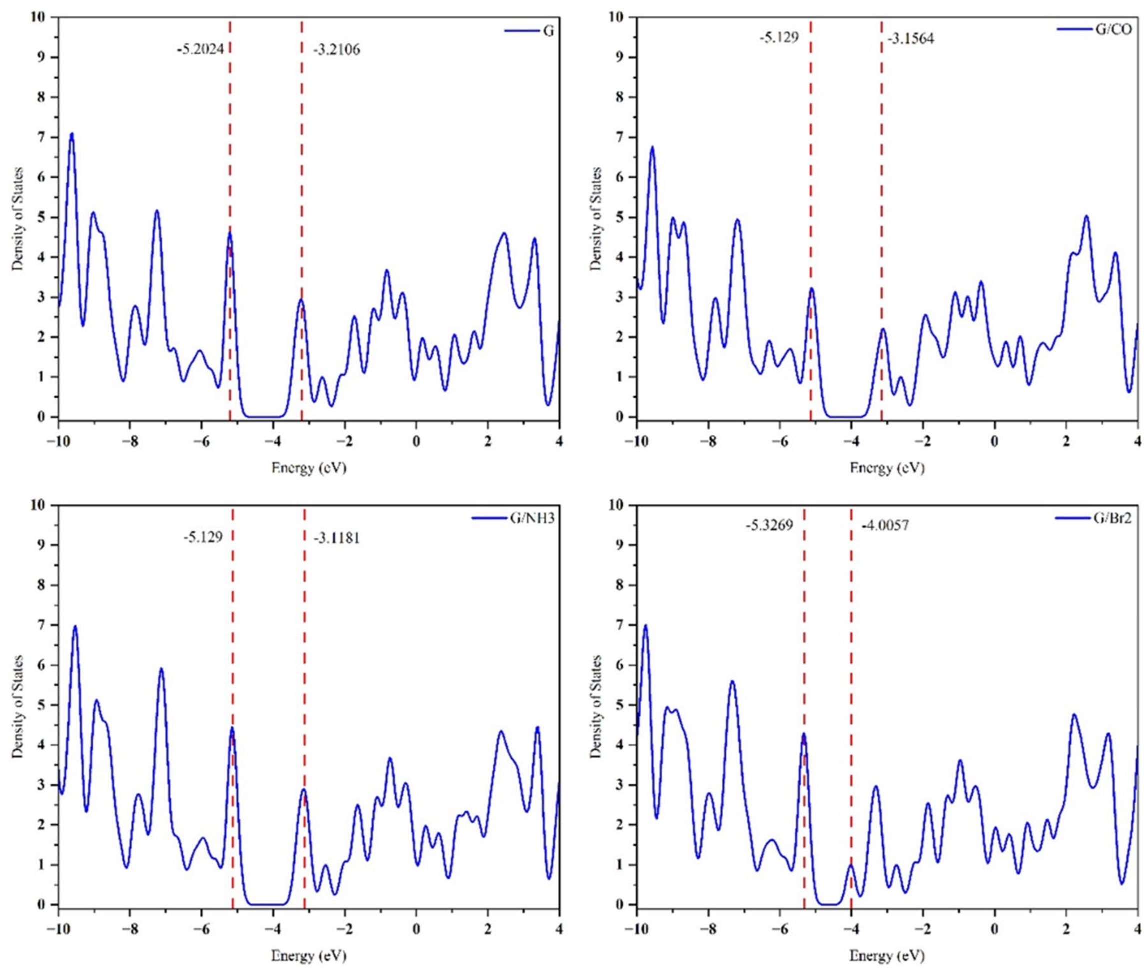

Fig. 5 The density of state (DOS) for the adsorption process between the gas molecule (CO, NH_3, and Br_2) and the surface of G nanostructure

The energy gap of SG shifted from 1.732 to 0.976 eV. Additionally, the reactivity of the SG surface for Br_2 is higher compared to other gases (NH_3 and CO). Consequently, the calculations deduced that doping the graphene nanostructure with S atoms enhanced the reactivity to NH_3 and CO. Furthermore, the doping mechanism enhances the reactivity of the graphene nanostructure, along with the curvature on the SG surface.

Figure 6 indexes the density of states (DOS) spectrum for the adsorption process between the surface of the GS nanostructure and gas molecules, with the energy range of the DOS spectrum spanning from − 10 to 4 eV. The DOS spectrum points out the shift in the molecular orbitals' energy during the adsorption process. From the DOS spectrum, it is observed that all HOMO molecular orbitals experience a slight shift to higher energy levels. For example, the HOMO level for GS shifted from − 5.099 to − 4.841 eV when Br_2 adsorbed on the surface of GS. Meanwhile, the calculations showed that all LUMO levels moved to lower energy levels during the adsorption process. For instance, the LUMO level shifted from − 3.367 to − 3.385 eV when Br_2 adsorbed on the surface of the GS nanostructure.

UV-visible spectrum

In this section, we aim to analyze the UV-visible spectrum of both G and GS nanostructures to investigate the influence of the adsorption process. The time-dependent density functional theory (TD-DFT) technique will be employed to study the UV-visible spectrum and determine the maximum absorption wavelength, with the number of transition states set to $N = 14$ [65]. The maximum absorption wavelengths, both in the presence and absence of gas molecules, will be compared for G and GS nanostructures, and the results will be presented in Fig. 7A, B, respectively. According to the data in Fig. 7A, the G nanostructure exhibits a maximum absorption wavelength of 810.25 nm [66], indicating absorption in the red region of the electromagnetic spectrum. Notably, the UV-visible spectrum undergoes a noticeable shift when gas molecules interact with the surface of the G

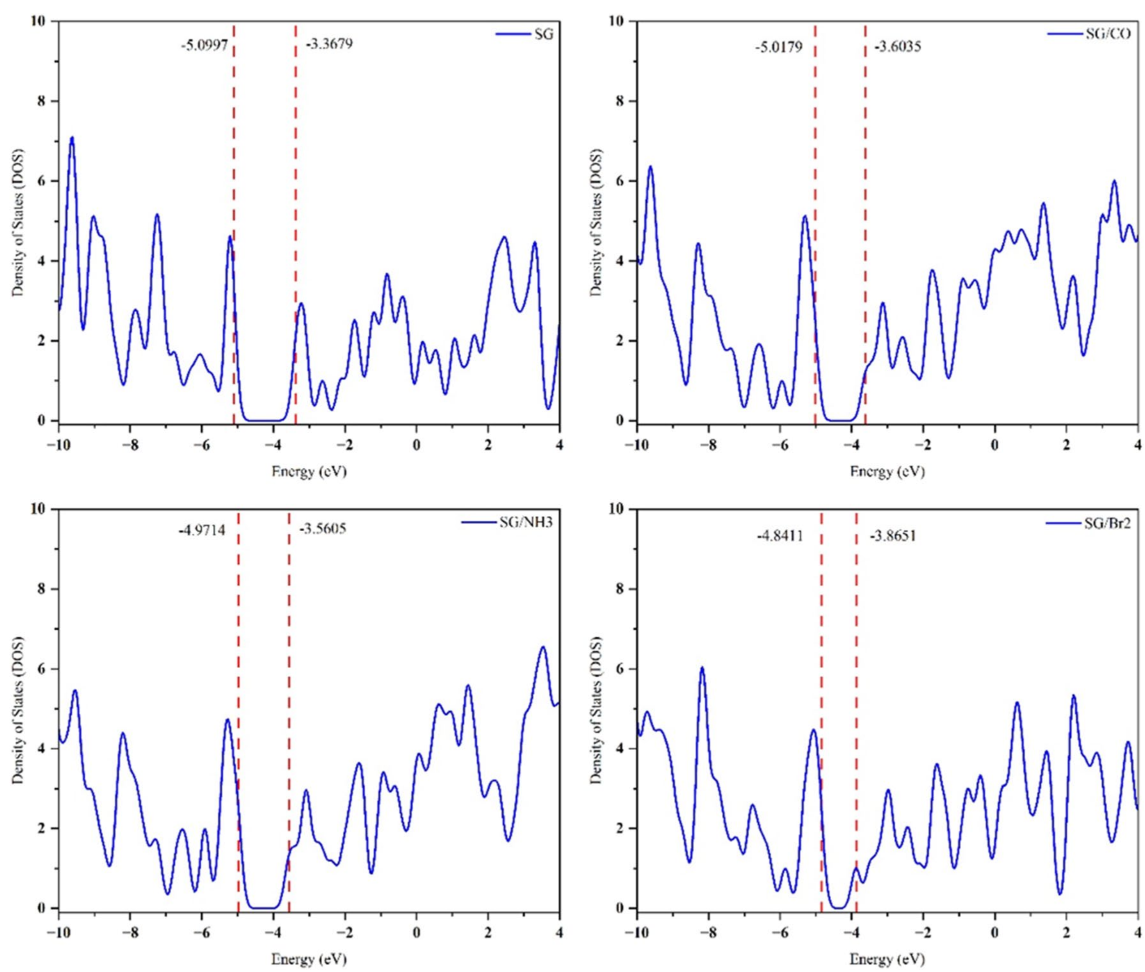

Fig. 6 The figurc indexed the DOS spectrum for the isolated and adsorbed phase of the GS nanostructure

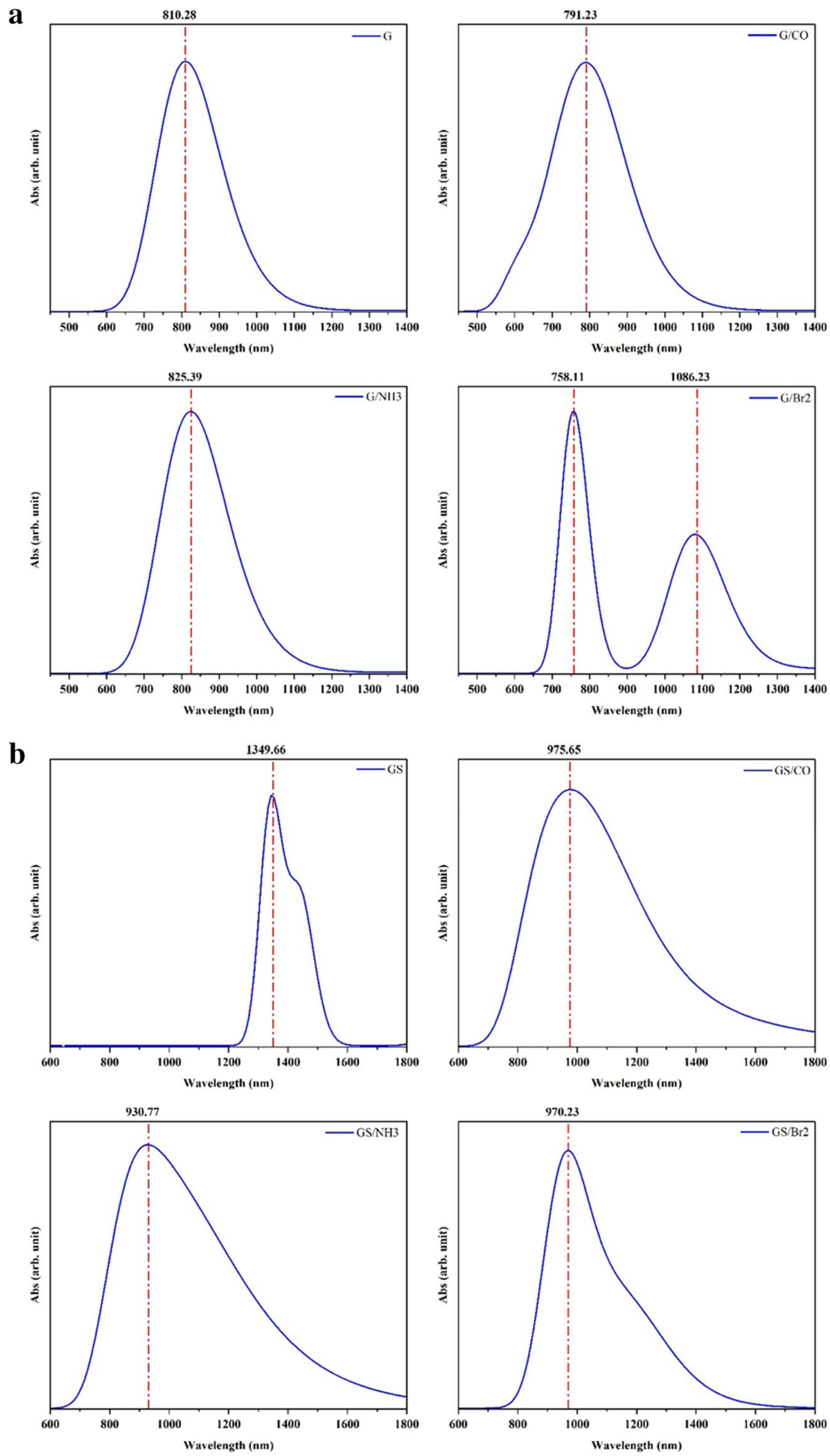

Fig. 7 **A** The UV-visible spectrum for G nanostructure in the isolated and adsorbed phase, respectively computed by TD-DFT tool. **B** The UV-visible spectrum for GS nanostructure in the isolated and adsorbed phase, respectively computed by TD-DFT method

nanostructure, as indicated in Fig. 7A. The interaction of Br_2 with the G nanostructure surface demonstrates significant chemical adsorption, as evidenced by the observed shift of the UV-visible spectrum towards the red region of the electromagnetic radiation.

The maximum absorption for the GS nanostructure has been found at a wavelength of 1349.66 nm [67]. The UV-visible spectrum of the graphene nanomaterial has shifted to the near-infrared (NIR) region of the electromagnetic radiation as a result of the doping treatment, as shown by the results [68]. The presence of S atoms has a direct impact on the UV-visible spectrum. Additionally, the UV-visible spectrum shifts to the red range of electromagnetic radiation when gas molecules are adsorbed on the surface of the GS nanostructure. The high chemical interaction between gas molecules and the surface of the GS nanostructure causes a shift in the UV-visible spectrum [12].

Renewable energy part

This section will estimate the probability of applying the graphene and S-doped nanostructure in the SSC device.

Electronic characteristics of G and GS nanostructures

To deduce the performance of the solar cell sensitizer, one of the most essential parameters is the population of molecular orbitals energy levels around the minimum conduction band of the titanium dioxide semiconductor and iodine/tri-iodine (I/I_3) electrolyte. To achieve electron injection and regeneration in the conduction band minimum (CBM) of the TiO2 semiconductor and I/I_3 electrolyte, two following criteria should be satisfied [69]:

1- All LUMO levels should localize above the $CBM_{(TiO2)}$ semiconductor, the $CBM_{(TiO2)}$ value is (− 4.3) eV.

2- All HOMO levels should distribute below the (I/I_3) electrolyte, the redox potential energy is (− 4.85) eV.

According to these two criteria conditions the solar cell sensitizer works in perfect phase [65].

Figure 8 illustrates the distribution of molecular orbital energy levels for the G and GS nanostructures around the conduction band minimum (CBM) of the TiO2 semiconductor and the iodine/tri-iodine (I/I_3) electrolyte. From this figure, the computed results deduce that all HOMO levels of the G and GS nanostructures are localized below the I/I_3 electrolyte [70]. Additionally, the LUMO energy levels are observed above the CBM of the TiO2 semiconductor. Consequently, the G and GS nanostructures have the ability to inject an electron from the excited state to the CBM of the TiO2 semiconductor. Furthermore, electrons can transfer to the ground state of the G and GS nanostructures because all HOMO levels are located below the I/I_3 electrolyte. Therefore, the injection and regeneration process will occur.

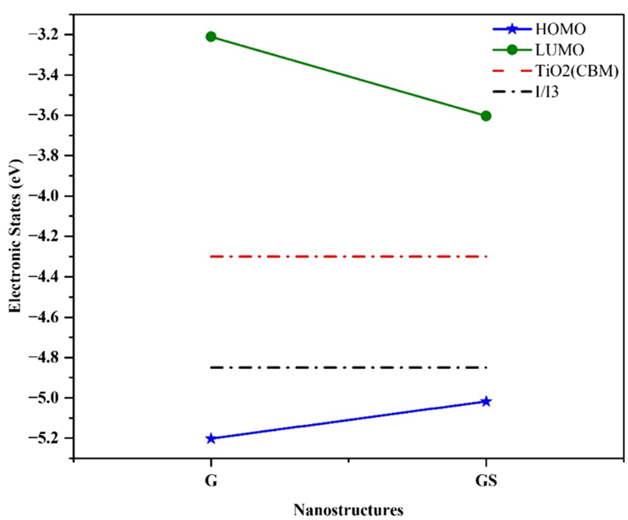

Fig. 8 Represent the distribution of molecular orbitals energy around the $CBM_{(TiO2)}$ and (I/I_3)

Graphene nanostructure sensitizer viability for solar sensitizer cells

The ideal cycle appears, when the electrons transfer from the higher molecular orbitals (HOMO) levels to lower molecular orbitals (LUMO) levels of the excited nanostructure inject into $CBM_{(TiO2)}$ semiconductor, spontaneously [71]. The photovoltaic parameters calculations involve the free energy of electron injection ($\Delta G_{\text{Injection}}$) and regeneration ($\Delta G_{\text{Regeneration}}$), open voltaic circuit (V_{OC}), maximum wavelength of absorption ($\lambda_{\max}$), excitation energy ($E_{OX}^{SSC^*}$) and oscillation strength (f) [72]. Table 6 summarizes the photovoltaic parameters for G and GS nanostructure computed by the DFT method. For both G and GS nanostructures, ($\Delta G_{\text{Injection}}$) observed in the negative range, as is present in Table 6. Consequently, the excited state of G and GS nanostructures localized above $CBM_{(TiO2)}$ semiconductor, for this reason, the electron will be injected from the excited state of nanostructures to $CBM_{(TiO2)}$.

Furthermore, the results showed that $\Delta G_{\text{Regeneration}}$ is a negative range, deduced that the redox level of the iodine/tri-iodine (I/I_3) electrolyte is lower than the stable state of the G and GS nanostructures. The lower value of free energy of electron regeneration and the higher value of free energy

Table 6 The free energy of electron injection ($\Delta G_{\text{Injection}}$), free energy of electron regeneration ($\Delta G_{\text{regeneration}}$), open-voltaic circuit (V_{OC}), maximum wavelength of absorption ($\lambda_{\max}$), excitation energy ($E_{\text{ox}}^{\text{dye*}}$) and oscillation strength (f)

Nanostructures	$\Delta G_{\text{Injection}}$ (eV)	$\Delta G_{\text{Regeneration}}$ (eV)	V_{OC} (eV)	$\lambda_{\max}$ (nm)	$E_{OX}^{SSC^*}$ (eV)	f
G	− 1.328	− 0.352	1.089	2.230	2.972	0.96
GS	− 0.392	− 0.249	0.932	1.399	3.701	0..35

of electron injection will deduce faster charge transport between the nanostructures and electrolytes [73].

Furthermore, the open voltaic circuit (V_{OC}) another essential parameter effect on the overall nanostructure efficiency. The (V_{OC}) for G and GS nanostructures calculated according to Eq. (7). The computed results showed that (V_{OC}) varied between 0.932 and 1.089 V, these values are sufficient for the ability of electron injection. The higher values of (V_{OC}) that is deduced in order to higher energy of lower molecular orbital level (E_{LUMO}), Consequently, the values of (V_{OC}) is proportional directly to (E_{LUMO}) [74].

UV-visible spectrum and LHE for G and GS nanostructures

The maximum wavelength of absorption and light harvesting efficiency for G and GS nanostructures were evaluated via the time-dependent density functional theory (TD-DFT) method, with a number of transition states set to $N = 30$. Figure 9 shows the UV-visible spectrum for G and GS nanostructures. The results deduced that the GS nanostructure has two absorption bands. The first peak is observed around 555.95 nm with an oscillation strength of 0.98, mainly formed by the transition HOMO→LUMO, and it represents the fundamental absorption band. The second absorption peak is found at 811.11 nm with an oscillation strength of 0.43, formed from the transition HOMO-1→LUMO+1. Additionally, the UV-visible spectrum deduced that the GS nanostructure has one absorption peak observed around 886.44 nm with an oscillation strength of 0.35, mainly formed from the transition HOMO→LUMO. Overall, adding S atoms to the surface of the graphene nanostructure affects the optical spectrum. Consequently, the fundamental peak of the G nanostructure shifted from 555.95 to 886.44 nm. Therefore, the UV-visible spectrum of the G nanostructure shifts to the lower energy region (redshift) when doped by four S atoms.

In addition to the open voltaic circuit, the maximum wavelength of absorption, and free energy of electron injection and regeneration, the light-harvesting efficiency (LHE) is another important parameter quantifying the efficiency of solar cell sensitizer. Figure 10 illustrates the bar chart of LHE for G and GS nanostructures. The computed results of LHE deduce that the G nanostructure has a high ability to harvest light compared with the GS nanostructure. The LHE of the G nanostructure is observed at around 89%, while for the GS nanostructure, it is around 55%. Altogether, the LHE results indicate that the nanostructures under investigation have a high response-ability for incident light.

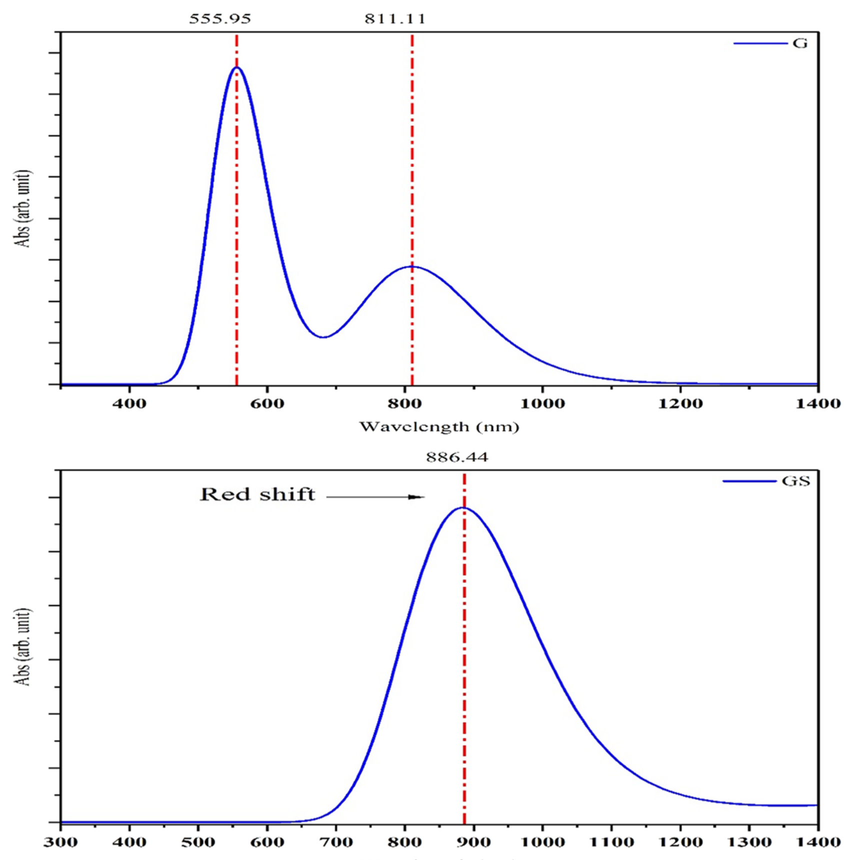

Fig. 9 The UV-visible spectrum for the G and GS nanostructures computed by the TD-DFT method

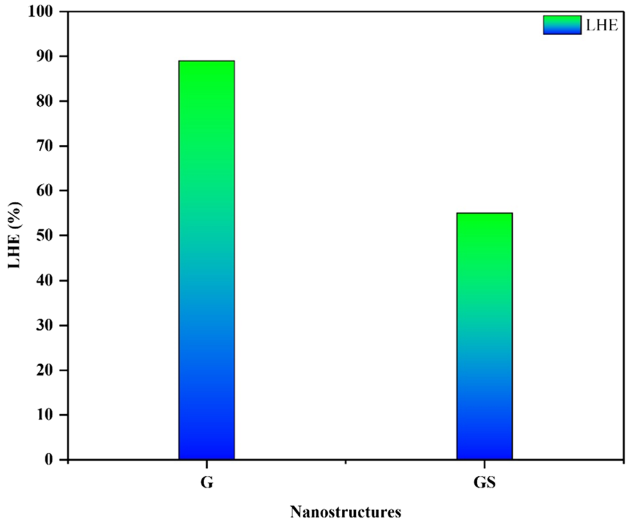

Fig. 10 Index the bar chart of the light-harvesting efficiency (LHE) for G and GS nanostructures

Conclusions

This study utilized ground state calculations at the B3LYP/6-31G* level to investigate the optimal structure and electrical characteristics of both pure and S-doped graphene nanostructures. The TD-DFT tool was employed to simulate the UV-visible spectrum and analyze the absorption properties. The results exhibited superior adsorption of Br2 gas molecules compared to CO and NH3. The incorporation of sulfur atoms into the graphene nanostructures improved the chemical interactions between CO and NH3, thereby enhancing the adsorption process. This highlights the significance of sulfur doping in modifying the interaction strengths between gas molecules and the surfaces of graphene nanostructures.

Moreover, both G and GS nanostructures displayed HOMO and LUMO energy levels that were compatible with the CBM(TiO2) electrode and iodine/tri-iodine electrolyte used in established SSC devices. This suggests that the LUMO of graphene and the S-doped nanostructure contribute to efficient charge transport to the CBM(TiO_2) electrode under the specified conditions. These findings provide valuable insights for the development of dye-sensitized solar cells (DSSC) and the construction of alternative materials for efficient sunlight harvesting. The results from the adsorption section revealed that pure graphene nanostructures. Overall, the study's findings contribute to a deeper understanding of the structural, electrical, and optical properties of pure and S-doped graphene nanostructures, emphasizing their potential for application in sustainable energy technologies such as solar cells.

Acknowledgements The authors would like to express gratitude to Dr. Mousumi for his invaluable assistance in making amendments to the research paper and providing insightful corrections. Dr. Mousumi's expertise and guidance have been instrumental in enhancing the quality of this work. I am thankful for their support and collaboration. Dr. Mousumi is affiliated with ELI-ALPS, ELI-HU Non-Profit Ltd., Wolfgang Sandner Utca 3, Szeged, Hungary, and the Department of Physics, University of Szeged, Szeged, Hungary.

Funding The authors declare that no funds, grants, or other support were received during the preparation of this manuscript.

Data availability Data sharing is not applicable to this article as no datasets were generated or analyzed during the current study.

Declarations

Ethics approval Not applicable.

Conflict of interest The authors declare that they have no conflicts of interest.

References

1. Abbasi A, Sardroodi JJ (2019) Adsorption of O3, SO2 and SO3 gas molecules on MoS2 monolayers: a computational investigation. Appl Surf Sci 469:781–791
2. Splendiani A et al (2010) Emerging photoluminescence in monolayer MoS2. Nano Lett 10(4):1271–1275
3. Fang H, Chuang S, Chang TC, Takei K, Takahashi T, Javey A (2012) High-performance single layered WSe2 p-FETs with chemically doped contacts. Nano Lett 12(7):3788–3792
4. Abbasi A, Sardroodi JJ (2017) An innovative gas sensor system designed from a sensitive nanostructured ZnO for the selective detection of SO x molecules: a density functional theory study. New J Chem 41(21):12569–12580
5. Abbasi A (2019) Adsorption of phenol, hydrazine and thiophene on stanene monolayers: a computational investigation. Synth Met 247:26–36
6. Drummond N, Zolyomi V, Fal'Ko V (2012) Electrically tunable band gap in silicene. Phys Rev B 85(7):075423
7. Xia W, Hu W, Li Z, Yang J (2014) A first-principles study of gas adsorption on germanene. Phys Chem Chem Phys 16(41):22495–22498
8. Kaloni TP (2014) Tuning the structural, electronic, and magnetic properties of germanene by the adsorption of 3d transition metal atoms. J Phys Chem C 118(43):25200–25208
9. Elías AL et al (2013) Controlled synthesis and transfer of large-area WS2 sheets: from single layer to few layers. ACS Nano 7(6):5235–5242
10. Abbasi A, Sardroodi JJ (2018) Density functional theory investigation of the interactions between the buckled stanene nanosheet and XO2 gases (X= N, S, C). Comput Theor Chem 1125:15–28
11. Balendhran S, Walia S, Nili H, Sriram S, Bhaskaran M (2015) Elemental analogues of graphene: silicene, germanene, stanene, and phosphorene. Small 11(6):640–652
12. Abbasi A, Sardroodi JJ (2019) The adsorption of sulfur trioxide and ozone molecules on stanene nanosheets investigated by DFT: Applications to gas sensor devices. Physica E 108:382–390
13. Cao S, Low J, Yu J, Jaroniec M (2015) Polymeric photocatalysts based on graphitic carbon nitride. Adv Mater 27(13):2150–2176
14. Storage CCE (2002) Liquid-mediated dense integration of graphene materials for. Adv Mater 14:1850–1853

15. Wang J, Xu Y, Zhang S-C (2014) Two-dimensional time-reversal-invariant topological superconductivity in a doped quantum spin-Hall insulator. Phys Rev B 90(5):054503
16. Abbasi A (2019) Theoretical investigation of the interaction between noble metals (Ag, Au, Pd, Pt) and stanene nanosheets: a DFT study. J Inorg Organomet Polym Mater 29(6):1895–1915
17. Abbasi A (2019) Modulation of the electronic properties of pristine and AlP-codoped stanene monolayers by the adsorption of CH2O and CH4 molecules: a DFT study. Mater Res Expr 6(7):076410
18. Baugher BW, Churchill HO, Yang Y, Jarillo-Herrero P (2014) Optoelectronic devices based on electrically tunable p–n diodes in a monolayer dichalcogenide. Nat Nanotechnol 9(4):262–267
19. Choudhuri I, Sadhukhan D, Garg P, Mahata A, Pathak B (2016) Lewis acid–base adducts for improving the selectivity and sensitivity of graphene based gas sensors. ACS Sensors 1(4):451–459
20. Choudhuri I, Patra N, Mahata A, Ahuja R, Pathak B (2015) B–N@Graphene: highly sensitive and selective gas sensor. J Phys Chem C 119(44):24827–24836
21. Hu W, Xia N, Wu X, Li Z, Yang J (2014) Silicene as a highly sensitive molecule sensor for NH 3, NO and NO 2. Phys Chem Chem Phys 16(15):6957–6962
22. Matei DG et al (2013) Functional single-layer graphene sheets from aromatic monolayers. Adv Mater 25(30):4146–4151
23. Ashok Kumar SS, Bashir S, Ramesh K, Ramesh S (2022) A review on graphene and its derivatives as the forerunner of the two-dimensional material family for the future. J Mater Sci 57(26):12236–12278
24. Liang Y, Zhou Y, Smith Jr RL, Qi X (2023) Ultra-thin highly-wrinkled graphene-like nanosheets for supercapacitor electrodes via 4-nitrocatechol and solvent-induced self-assembly. Carbon 204:495–506
25. Giovannetti G, Capone M, van den Brink J, Ortix C (2015) Kekulé textures, pseudospin-one Dirac cones, and quadratic band crossings in a graphene-hexagonal indium chalcogenide bilayer. Phys Rev B 91(12):121417
26. Gao J-H, Ishida N, Scott I, Fujita D (2012) Controllable growth of single-layer graphene on a Pd (1 1 1) substrate. Carbon 50(4):1674–1680
27. Mukhopadhyay T, Mahata A, Adhikari S, Zaeem MA (2018) Probing the shear modulus of two-dimensional multiplanar nanostructures and heterostructures. Nanoscale 10(11):5280–5294
28. Talukder N, Wang Y, Nunna BB, Lee ES (2021) Nitrogen-doped graphene nanomaterials for electrochemical catalysis/reactions: a review on chemical structures and stability. Carbon 185:198–214
29. Mohan P, Ghorai U, Sensarma R (2021) Trigonal warping, satellite dirac points, and multiple field tuned topological transitions in twisted double bilayer graphene. Physical Rev B 103(15):155149
30. Kaloni TP, Kahaly MU, Cheng Y, Schwingenschlögl U (2012) Ge-intercalated graphene: The origin of the p-type to n-type transition. Europhys Lett 99(5):57002
31. Upadhyay Kahaly M, Misra S, Mishra S (2017) Photo-assisted electron emission from illuminated monolayer graphene. J Appl Phys 121(20). https://doi.org/10.1063/1.4984318
32. Mishra SK, Kahaly MU, Misra S (2017) Efficient utilization of multilayer graphene towards thermionic convertors. Int J Therm Sci 121:358–368
33. Jin Y, Zheng Y, Podkolzin SG, Lee W (2020) Band gap of reduced graphene oxide tuned by controlling functional groups. J Mater Chem C 8(14):4885–4894
34. Kahaly MU (2009) Defect states in carbon nanotubes and related band structure engineering: A first-principles study. J Appl Phys 105(2). https://doi.org/10.1063/1.3072695
35. Upadhyay Kahaly M, Waghmare UV (2007) Size dependence of thermal properties of armchair carbon nanotubes: a first-principles study. Appl Phys Lett 91(2). https://doi.org/10.1063/1.2753095
36. Sharma A, Singh A, Gupta V, Sundramoorthy AK, Arya S (2023) Involvement of metal organic frameworks in wearable electrochemical sensor for efficient performance. Trends Environ Anal Chem 38:e00200
37. Demon SZN et al (2020) Graphene-based materials in gas sensor applications: a review. Sens Mater 32:759–777
38. Kaushal S, Kaur M, Kaur N, Kumari V, Singh PP (2020) Heteroatom-doped graphene as sensing materials: a mini review. RSC Adv 10(48):28608–28629
39. Jiang B, Wang S, Sun J, Liu Z (2021) Controllable synthesis of wafer-scale graphene films: challenges, status, and perspectives. Small 17(37):2008017
40. Sacchi M, Tamtögl A (2023) Water adsorption and dynamics on graphene and other 2D materials: Computational and experimental advances. Adv Phys: X 8(1):–2134051
41. Raad NH, Manavizadeh N, Frank I, Nadimi E (2021) Gas sensing properties of a two-dimensional graphene/h-BN multi-heterostructure toward H2O, NH3 and NO2: A first principles study. Appl Surf Sci 565:150454
42. Elavarasan RM, Afridhis S, Vijayaraghavan RR, Subramaniam U, Nurunnabi M (2020) SWOT analysis: a framework for comprehensive evaluation of drivers and barriers for renewable energy development in significant countries. Energy Rep 6:1838–1864
43. Devadiga D, Selvakumar M, Shetty P, Santosh M (2021) Recent progress in dye sensitized solar cell materials and photo-supercapacitors: a review. J Power Sources 493:229698
44. Murugadoss G, Chinnakutti KK, Manibalan G, Manavalan RK, Brindhadevi K, Pugazhendhi A (2023) Cost-effective carbon black-graphite composite with solid-state based CuSCN electrode for dye-sensitized solar cells. Fuel 348:128527
45. Prajapat K, Dhonde M, Sahu K, Bhojane P, Murty V, Shirage PM (2023) The evolution of organic materials for efficient dye-sensitized solar cells. J Photochem Photobiol C: Photochem Rev:100586. https://doi.org/10.1016/j.jphotochemrev.2023.100586
46. Zhang J-Z et al (2014) Modulation on charge recombination and light harvesting toward high-performance benzothiadiazole-based sensitizers in dye-sensitized solar cells: a theoretical investigation. J Power Sources 267:300–308
47. Jain N et al (2021) Ruthenium (II) complexes bearing heteroleptic terpyridine ligands: synthesis, photophysics and solar energy conversion. Eur J Inorg Chem 2021(47):5014–5023
48. Zolghadr AR, Estakhr O, Heydari Dokoohaki M, Salari H (2021) Comparison between Bi2WO6 and TiO2 photoanodes in dye-sensitized solar cells: experimental and computational studies. Ind Eng Chem Res 60(33):12292–12306
49. Kadhim QS et al (2022) Effect of metal ad-atoms on the structural, electrical, and optical properties of boron-nitride nanostructures towards optoelectronics: a DFT based study. Egypt J Chem 65(13):745–752
50. Jiao Y, Zhang F, Meng S, Kosyachenko L (2011) Dye sensitized solar cells principles and new design. Solar Cells-Dye-Sensitized Devices 1(1)
51. Gajda Ł et al (2019) Spectroscopic characterization of non-covalent CuPc-GO system. Experiment and theory. Mater Chem Phys 231:301–310
52. Al-Seady MA et al (2023) Prospective utilization of boron nitride and beryllium oxide nanotubes for Na, Li, and K-ion batteries: a DFT-based analysis. J Mol Model 29(11):1–20
53. Al-Seady MA, Abdul Wahhab NA, Abbood HI, Abduljlil HM DFT study of chemical adsorption of NO2 gas on graphene nano material. Materials Science Forum, 2021, vol. 1039. Trans Tech Publ, pp 391–397
54. Al-Seady MA, Ahmed E, Abduljalil HM, Kahewish AA-R (2021) Studying the adsorption energy of CO gas molecule in

different nano-systems using density function theory. Egypt J Chem 64(5):2607–2612
55. Abbasi A, Khataee A (2019) Band gap tunability and structural stability of metal/nonmetal codoped group-IV tin nanotubes: effect of spin-orbit coupling. Physica E 114:113644
56. Mohammad RK, Nowfal SH, Al-Seady MA, Abduljalild HM (2022) Investigation ability of single walled carbon nanotubes to detection toxic gases utilizing DFT Calculations. Egypt J Chem 65(6):89–98
57. Madlol HA et al (2022) Comparative adsorption calculations for carbon mono-oxide and hydro cyanide gas molecules interaction with graphene material using density function theory. Egypt J Chem 65(131):385–391
58. Mohammed HT, Kamil AM, Abduljalil HM, Abbas A, Drea A, Al-Seady MA (2023) Degradation of indigo dye using quantum mechanical calculations. Baghdad Sci J 20(4):1352
59. Inah BE et al (2023) Adsorption and gas-sensing investigation of oil dissolved gases onto nitrogen and sulfur doped graphene quantum dots. Chem Phys Impact 7:100265
60. Al-Seady MA, Grmasha RA, Al-Aaraji NA-H, Abduljalil HM (2021) Investigation adsorption mechanism of methane gas in graphene and copper doped nano-ribbon using density function theory. J Phys: Conf Ser 1879(3):032099
61. Cui H, Jia P (2020) Doping effect of small Rhn (n= 1–4) clusters on the geometric and electronic behaviors of MoS2 monolayer: a first-principles study. Appl Surf Sci 526:146659
62. S. A. Jasim, E. Ahmed, S. M. Al-Ghazaly, M. A. Al-Seady, and H. M. Abduljalil, Study adsorption ability of pure single walled carbon nano tube to detection some toxic gases using DFT calculation, in AIP Conference Proceedings, 2022, vol. 2398, no. 1: AIP Publishing.
63. N. A.-H. Al-Aaraji et al., Investigation the ability of pure and Al-doped graphene nano materials to detect toxic gases using first principle study, in IOP Conference Series: Earth and Environmental Science, 2022, vol. 1088, no. 1: IOP Publishing 012013.
64. Udoikono AD et al (2022) Reactive azo compounds as a potential chemotherapy drugs in the treatment of malignant glioblastoma (GBM): Experimental and theoretical studies. J Photochem Photobiol 10:100116
65. H. H. Abed, N. A.-H. Al-Aaraji, J. M. Salman, H. M. Abduljalil, and M. A. Al-Seady, Theoretical study on dye-sensitized solar cells using graphene quantum dot and curcumin, pahthalocyanine dyes, in IOP Conference Series: Earth and Environmental Science, 2022, vol. 1088, no. 1: IOP Publishing 012012.
66. Manoratne C, Rosa S, Kottegoda I (2017) XRD-HTA, UV visible, FTIR and SEM interpretation of reduced graphene oxide synthesized from high purity vein graphite. Mater Sci Res India 14(1):19–30
67. Mandal B, Sarkar S, Sarkar P (2015) Theoretical studies on understanding the feasibility of porphyrin-sensitized graphene quantum dot solar cell. J Phys Chem C 119(6):3400–3407
68. Li Y, Shu H, Niu X, Wang J (2015) Electronic and optical properties of edge-functionalized graphene quantum dots and the underlying mechanism. J Phys Chem C 119(44):24950–24957
69. Prabavathy N, Shalini S, Balasundaraprabhu R, Velauthapillai D, Prasanna S, Muthukumarasamy N (2017) Enhancement in the photostability of natural dyes for dye-sensitized solar cell (DSSC) applications: a review. Int J Energy Res 41(10):1372–1396
70. Pandey A, Ahmad MS, Rahim NA, Tyagi V, Saidur R (2019) Natural sensitizers and their applications in dye-sensitized solar cell. Environmental biotechnology: for sustainable future. Springer, pp 375–401
71. Patni N, Pillai SG, Sharma P (2020) Effect of using betalain, anthocyanin and chlorophyll dyes together as a sensitizer on enhancing the efficiency of dye-sensitized solar cell. Int J Energy Res 44(13):10846–10859
72. Faiz MR, Widhiyanuriyawan D, Siswanto E, Wardana I (2017) Theoretical study on the application of natural green pigment for sensitizer in dye-sensitized solar cell (DSSC). 2017 5th International Conference on Electrical, Electronics and Information Engineering (ICEEIE). IEEE, pp 32–37
73. Bevilacqua AC, Köhler MH, Iglesias BA, Piquini PC (2019) Photophysical and photocatalytic properties of corrophyll and chlorophyll. Comput Mater Sci 158:228–234
74. Liu Q, Gao N, Liu D, Liu J, Li Y (2018) Structure and photoelectrical properties of natural photoactive dyes for solar cells. Appl Sci 8(9):1697